CFD simulation of the hydrodynamics within an RVF module in laminar regime

Ming CHENG[1], Luc FILLAUDEAU[1,2], Philippe SCHMITZ[1,2]

[1]TBI, Université de Toulouse, CNRS UMR5504, INRA UMR792, INSA, 31055, 135, avenue de Rangueil, Toulouse, France

[2]Federation de Recherche FERMAT (FR 3089), Université de Toulouse, CNRS, INPT, INSA, UPS, Toulouse, France

Abstract: The dynamic filtration module called Rotating and Vibrating Filtration (RVF) is a performant device for membrane fouling control and limiting the formation of cake layer. Indeed, it can generate strong shear stress at the membrane surface decoupled from the feeding flowrate. Moreover, the pressure fluctuation that takes place in the device is also beneficial to control membrane fouling. A CFD model has been validated in laminar regime from experimental measurements of velocity fields and pressure distribution inside the RVF. The boundary layer development at the walls were carefully studied to better explain the effects of the rotation speed and the viscosity on the spatial distribution and time variations of pressure and shear stress at the membrane surface. It appears that shear stress is more efficient than pressure to control membrane performances in laminar regime.

Keywords: RVF, CFD, hydrodynamics behaviour, laminar regime

INTRODUCTION

Membrane bioreactors (MBR) are now largely applied in biotechnology (e.g., food biotechnology, environmental, industry, health, etc.) [1-3]. Then, dynamic filtration (DF) stands as a highly relevant alternative to classical filtration techniques such as dead-end and crossflow filtrations. Indeed, it can be considered a more efficient filtration technology for the high mechanical shear stress at the membrane surface [4]. Its high efficiency and relatively energy-saving advantages make it widely used in water treatment, food processing and biological processes. An extensive review about DF listed 55 identified modules and their applications to show the difference strategies in enhancing membrane shear stress [5].

CFD techniques predict the flow field by solving basic governing equations such as mass, momentum and continuity equations instead of requiring complex experiments. Ladeg et.al [18] reported the performance of flow inside a RDM with CFD. They found the highest pressures were obtained by using disks equipped with vanes rather than disk, since the vanes created additional turbulent along the membrane surface. Hwang et al. [19] also confirmed this view. Four vans exhibited the higher filtration performance and the lowest cake resistance than two vans, but it generates more energy consumption at the same time [20, 21]. Ratkovich et al. [21] compare the experimental and CFD simulation of wall shear stress for different impeller configurations and MBR activated sludge. It shows good agreement between the electrochemical approach and CFD simulations (<9% error). But the former case cannot be achieved with non-Newtonian behaviour of activated sludge. An empirical relationship was established to determine the area-weighted average shear stress as a function of the angular velocity (in rpm) and the total suspended solid [22].

The hydrodynamics inside RVF have been investigated in the previous study to identify the pressure and velocity distribution [16, 23, 24]. The current study presents a CFD simulation of flow induced by a rotating impeller under laminar regime. Different concentrations of BREOX solutions as Newtonian fluid were modelled. Pressure, velocity and shear stress evolutions have been calculated under varying operating parameters (viscosity, rotation speed). All the simulations were performed without permeation. These results help us to better understand the fluid flow in the filtration cell, and give the new insight into optimizing the cell design.

MATERIALS AND METHODS

Computational domain

The lab-scale RVF module consists of two cylindrical filtration cells in series. Each of them comprises an impeller with three blades regularly spaced of 120°. Assuming that the two cells work identically, only one cell is considered. Moreover, the computational domain is limited to one-third of the cell with periodic boundary conditions, as shown in Fig. 1.

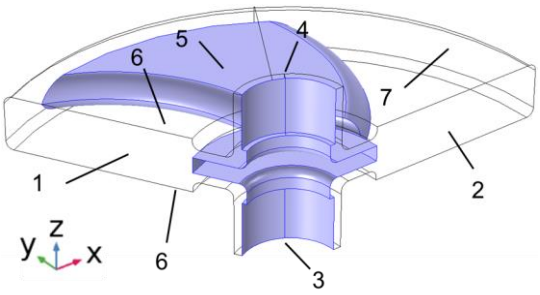

Fig. 1 Schematic of RVF cell (impeller RVF and cell housing). 1-2: Periodic flow cross-section (in/ out); 3-4: feeding inlet/ outlet; 5: impeller RVF; 6: membrane; 7: surrounding wall.

Model and fluids

It is assumed that the fluid is Newtonian, incompressible, and isothermal. The local mass and momentum balances are governed by the Navier Stokes (N-S) equations expressed in a fixed reference frame. Thus, the steady-state flow is solved under the laminar regime.

Boundary conditions

Fig. 1 shows the configurations of RVF cell. An impeller (r=67.5 mm) rotates with the central shaft (r=12 mm) at a constant rotation speed (*N*) inside a cylindrical housing (r=71 mm). The fluid flows along the central shaft at the bottom and leaves at the upper end. We define the *xy*-axis parallel to the plane of the impeller and the *z*-axis along the direction of rotation. On the other hand, the cylindrical coordinate is also defined in the geometry: θ and *r* indicate the angular and radial components, respectively.

The simulations are carried out under the following conditions (Fig. 1):

(1) The flow is assumed to be periodic in the angular direction (sections 1 and 2);

(2) Periodic boundary conditions are also used at the inlet and outlet faces (3-4). Here an average pressure gradient in the *z*-direction is imposed, which magnitude is adjusted to get the expected flowrate, *Q*;

(3) A reference pressure constraint point at the outlet face (4) is set as the back pressure, P_b;
(4) A no-slip boundary condition is imposed at both walls: the velocity is zero at membrane surfaces (6) and surrounding walls (7), the velocity is equal to $2\pi Nr$ in the θ direction at both blade and shaft walls (5) to account for the rotation of the impeller.

Mesh

The so-called "normal" mesh is generated automatically with COMSOL 5.5 based on the physics. Different element types such as tetrahedral, pyramid, prism, triangular, quadrilateral, edge and vertex elements are then generated, resulting in the 299510 domain cells, 32242 boundary elements and 2401 edge cells for impeller RVF in the filtration cell (1/3).

Operating parameters

The experimental set-up and data acquisitions have already been realised in a previous work to study the local and instantaneous pressure in turbulent regime [23, 24]. The same work was achieved in laminar regime with BREOX solution to validate the model. BREOX solution with a viscosity ranging from 0.05 to 0.6 Pa.s, are assumed to be incompressible and independent of temperature. The back pressure (P_b) fixed at constant values of 300 mbar and flowrate (Q) around 25 L/h. The impeller rotation speed (N) varied from 0 to 50 Hz so that the maximum mixing Reynolds number (Re_{mixing}) could reach 18800, which is in the laminar regime [5, 25].

RESULTS AND DISCUSSION

Validation of the model

In order to verify the reliability of COMSOL for the flow simulation within the RVF, we compared the fluid flow velocity and pressure obtained numerically with the experimental results, respectively. Table. 1 presents the operating conditions for the validation.

Table. 1 Validation of CFD simulation based on velocity and pressure field.

Simulation	Fluid properties		Operating parameters		
	ρ (kg/m^3)	μ (Pa.s)	N (Hz)	P_b (mbar)	Q (L/h)
Velocity	1060	0.81	2	300	45
Pressure	1060	0.18	0-30	625	25

The velocity profile in the RVF module has been investigated with PIV technology in a previous study [26]. The magnitude of the horizontal velocity component (*xy*-plane) along the *z*-axis, which is mainly in the θ direction, is shown in Fig. 2 a. Different θ positions were explored regarding the impeller position: leading, middle and trailing. The horizontal velocity significantly increases when close to the blades. Considering the PIV measurements as the reference, the velocity is well calculated by the CFD model at the leading edge, while it is slightly overestimated between two blades and at the trailing edge. It should be noted that the numerical results also show large deviations in the impeller zone ($-4<z<4$ mm). This can be explained by the influence of the impeller on the laser during the PIV measurement, where the velocity values can only be determined between the two blades. Nevertheless, it can be claimed that the numerical velocity profiles are in great agreement with the experimental

results if the deviations in the laser installation process are considered.

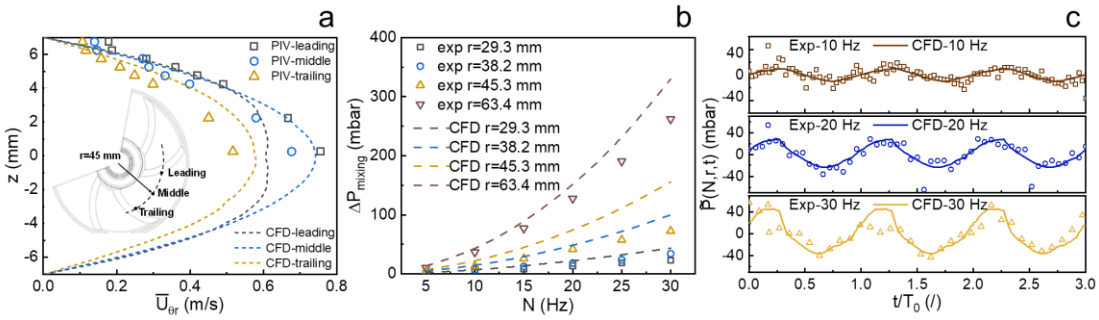

Fig. 2 Validation of CFD (a) Horizontal velocity profile at z-direction and r=45 mm for PIV measurement and CFD simulation; (b) and (c) are the mean mixing pressure and its fluctuating component versus rotation speed.

The local pressure *P* at the membrane surface can be decomposed into stationary pressure P_0, mixing pressure ΔP_{mixing} and pressure fluctuation $\tilde{P}(N,r,t)$. The former is governed by back pressure, whereas the latter two varies with time, rotation speed N and position (*r* and θ). The comparison of the pressure obtained numerically and the experimental measurements can be seen in Fig. 2 b and c. The mixing pressure tends to increase with N, the gap between CFD results and experimental data also increases, as can be seen in Fig. 2 b. It should be mentioned that the simulations were carried out in ideal conditions, and the temperature variations due to high friction were not considered. For pressure fluctuation, three periods ($3T_0$) of experimental data and CFD results are presented in Fig. 2 c. Here the angle θ variable was replaced by the time *t* variable according to the following equation: $t = \frac{3\theta}{2\pi} T_0$, where T_0 is equal to $\frac{1}{N}$. The pressure fluctuations including the amplitude and the period of the signal, appears to be well reproduced by the model.

The CFD model being validated, further simulations can be carried out for a large range of operating conditions and different geometrical parameters.

Flow field analysis

Velocity

Fig. 3 a depicts the vertical profiles (*z*-axis) of the tangential velocity component U_θ at different locations in the cell relative to the position of the impeller (zone A-G can be seen in the figure). At the same radius (zone A, B and D, *r=60* mm), the tangential velocity varies with the location relative to the position of the impeller. The fluid velocity at the leading edge (zone B) remains identical to the impeller velocity close to the centre of the cell (*z=0* mm). On the contrary, it reaches its minimum value in the centre at the trailing edge (zone D). In the region of the narrow gap between the membrane and the blade, the vertical profile of the tangential velocity is roughly linearly from the membrane to the blade surface (zone C, E, F and G). A perfectly straight line would correspond to a Couette flow. Between the two blades, the velocity profile is almost parabolic (zone A). An exact parabolic shape would correspond to a Poiseuille flow. The maximum velocity value is around 7.5 m/s at zone B. It is close to the value

of $2\pi Nr$, which is the linear velocity of the blade at this radial position.

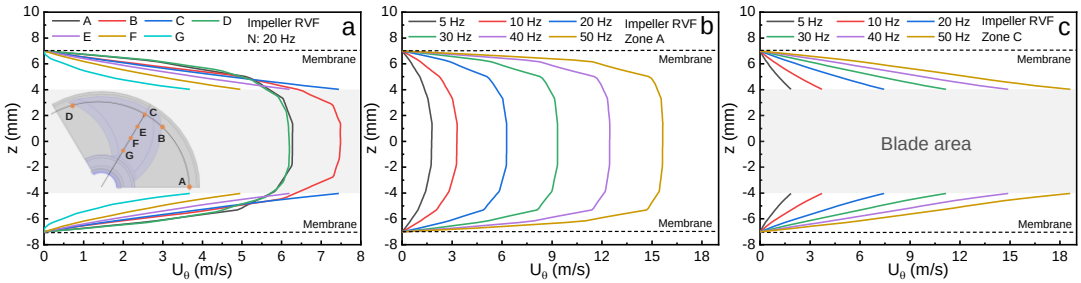

Fig. 3 Tangential velocity along the z-direction. (a) is the velocity distribution at different positions; (b) and (c) are the velocity distribution for different mixing rates at A and C, respectively. A (between two blades), B (leading edge), C (on the blade) and D (trailing edge) with a radius of 60 mm; E, F and G with a radius of 50, 40 and 30 mm, respectively.

It is really interesting to notice that the flow is not always fully developed; it depends on the *N* magnitude. At 5 or 10 Hz, it is fully developed (Poiseuille flow); this is proved by the perfect parabolic velocity profile. But it is not true for higher *N* values: boundary layer profile close to the wall and uniform velocity in the core region. The same analysis can be done in the region above/ below the blade (zone C). Fig. 3 c well exhibits that the fluid flow is not fully developed (Couette flow). One can physically understand that the higher *N*, the shorter time for the fluid flow to develop.

As we know that the kinematic viscosity is the momentum diffusion coefficient, we can simply deduce that the higher the viscosity, the easier the fluid to develop. This physical phenomenon is exactly reported in Fig. 4 a and b, where the vertical profiles of the tangential velocity are plotted for a large range of viscosity (0.05 to 0.6 Pa.s

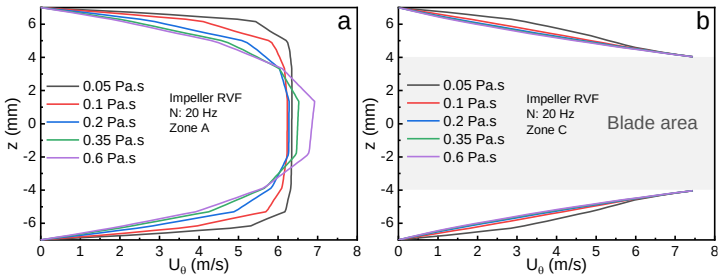

Fig. 4 Tangential velocity along the z-direction. (a) and (b) are velocity distribution at different positions for Imp 1.

Pressure

The effect of the operating conditions on the pressure variations has been clearly exemplified experimentally in turbulent regime [24]. We denote the mixing pressure and the magnitude of pressure fluctuations induced by the impeller with ΔP_{mixing} and σ_P, respectively. The rotation speed and the fluid viscosity appear as the key factors in controlling pressure fluctuations for process intensification in the application of the RVF module.

Fig. 5 shows the pressure field at the membrane surface and two different angular cross-sectionals (0 and 60° correspond to the black and red line, respectively). From the top view

(Fig. 5 c), the pressure is non-uniformly distributed at the membrane surface, and the maximum value occurs between two blades and close to the external wall. It is also seen that the pressure distribution is uniform in the vertical direction (Fig. 5 b and c) according to the type of flows occurring within the RVF (laminar boundary layer), which are already discussed in **0**.

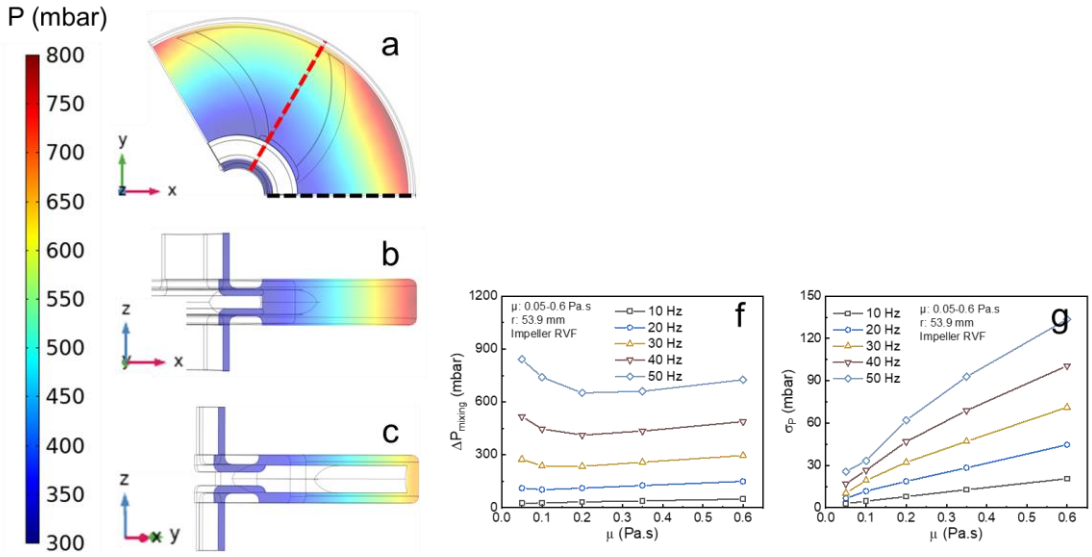

Fig. 5 Pressure field with impeller RVF. The pressure distribution are shown as top view (a), 0° cross-section (b) and 60° cross-section (c); (f) and (g) are the mixing pressure and its standard deviation.

The viscous effects on local pressure are illustrated in Fig. 5 f. At the same radius, the mixing pressures show a minimum value with the viscosity around 0.2 Pa.s. σ_P increases with the increasing viscosity, as presented in Fig. 5. Pressure fluctuation value is less than 13% of the TMP under laminar flow conditions.

Shear stress

The shear stress fields in different cross-sections of the filtration cell are shown in Fig. 6 a, b and c. At the membrane surface (Fig. 6 a), the maximum shear stress occurs at the trailing edge of the blades, which is exactly opposite to the pressure distribution. In the narrow gap between the impeller and the membrane , the boundary layer can merge together depending on the magnitude of *N*, resulting in slight variations of the shear stress along the *z*-direction (Fig. 6 c). While between the two blades, the large gap allows the separating boundary layer. The shear stress appears to reach the maximum at the membrane surface, and it is obviously about 0 close to the center of the cell between two blades (Fig. 6 b).

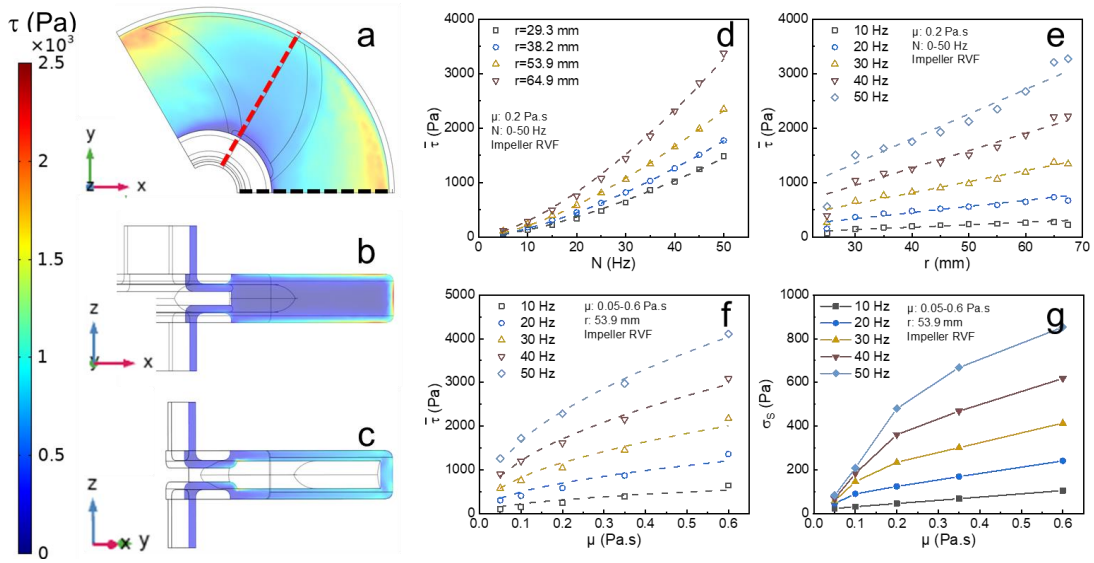

Fig. 6 Shear stress field with impeller RVF. The shear stress distribution are shown as top view (a), 0°cross-section (b) and 60°cross-section (c); (d) and (f) are the mean shear stress at the membrane surface; (g) is the standard deviation of local shear stress.

The shear stress variations as a function of the mixing rate are shown in Fig. 6 d, which indicates that the mean shear stress is linear with $N^{1.5}$. As can be seen from Fig. 6 e, the mean shear stress grows linearly with the radius. It is consistent with the work of Bourerar et al. [10] Contrary to pressure, the time-average shear stress increases with fluid viscosity in the rotating impeller device. It is proportional to $\mu^{0.5}$, as shown in Fig. 6 f. Thus, the following equation can be stated in the rotating impeller system, Eq. (1). Meantime, σ_s also increases with higher viscosity, as can be seen in Fig. 6 g.

$$\bar{\tau} = 0.96\rho^{0.5}\mu^{0.5}(2\pi kN)^{1.5}r, \text{ k=0.69} \quad (1)$$

CONCLUSIONS

Numerical simulations of the fluid flow within the RVF module in laminar regime were performed. Experimental results of velocity from PIV measurements and pressure distributions have been used to validate the CFD model. Thus, the velocity field, pressure and shear stress distribution at the membrane surface were carefully analysed to reveal the fluid boundary layer, and to highlight the best operating conditions.

The development of the boundary layers and subsequent spatial and time variations of pressure and shear stress at the membrane surface highly depends on the viscosity and the rotation speed. Under laminar regime (Re_{mixing}<20000), the pressure fluctuation (σ_P) is still less than 13% of the TMP (P_b=300 mbar), while shear stress fluctuation (σ_S) can reach more than 20% of its mean values in some cases. Therefore, the maximum value of the shear stress could be a pertinent criterion to achieve the optimal impeller design.

ACKNOWLEDGMENTS

Financial support from the China Scholarship Council is gratefully acknowledged (grant No. 201801810069).

REFERENCES

[1] W.H. Smith, Germination of Macrophomina phaseoli sclerotia as effected by Pinus lambertiana root exudate, Can J Microbiol, 15 (1969) 1387-1391.

[2] P. Aimar, G. Daufin, Séparations par membrane dans l'industrie alimentaire, F3250, Techniques de l'ingénieur, (2004) 1-23.

[3] G. Daufin, J.P. Escudier, H. Carrère, S. Bérot, L. Fillaudeau, M. Decloux, Recent and Emerging Applications of Membrane Processes in the Food and Dairy Industry, Food and Bioproducts Processing, 79 (2001) 89-102.

[4] M.Y. Jaffrin, Dynamic shear-enhanced membrane filtration: A review of rotating disks, rotating membranes and vibrating systems, Journal of Membrane Science, 324 (2008) 7-25.

[5] M. Cheng, X. Xie, P. Schmitz, L. Fillaudeau, Extensive review about industrial and laboratory dynamic filtration modules: Scientific production, configurations and performances, Separation and Purification Technology, 265 (2021) 118293.

[6] S. Ladeg, Z. Zhu, N. Moulai-Mostefa, L. Ding, M.Y. Jaffrin, CFD Simulation of the Distribution of Pressure and Shear Rate on the Surface of Rotating Membrane Equipped with Vanes for the Ultrafiltration of Dairy Effluent, Arabian Journal for Science and Engineering, 43 (2017) 2237-2245.

[7] K.-J. Hwang, S.-E. Wu, Disk structure on the performance of a rotating-disk dynamic filter: A case study on microalgae microfiltration, Chemical Engineering Research and Design, 94 (2015) 44-51.

[8] S.-E. Wu, K.-J. Hwang, T.-W. Cheng, K.-L. Tung, E. Iritani, N. Katagiri, Structural design of a rotating disk dynamic microfilter in improving filtration performance for fine particle removal, Journal of the Taiwan Institute of Chemical Engineers, 94 (2019) 43-52.

[9] N. Ratkovich, C.C.V. Chan, T.R. Bentzen, M.R. Rasmussen, Experimental and CFD simulation studies of wall shear stress for different impeller configurations and MBR activated sludge, Water Sci. Technol., 65 (2012) 2061-2070.

[10] T.R. Bentzen, N. Ratkovich, S. Madsen, J.C. Jensen, S.N. Bak, M.R. Rasmussen, Analytical and numerical modelling of Newtonian and non-Newtonian liquid in a rotational cross-flow MBR, Water Sci Technol, 66 (2012) 2318-2327.

[11] M. Cheng, C. Le Men, A. Line, P. Schmitz, L. Fillaudeau, Methodology to investigate instantaneous and local transmembrane pressure within Rotating and Vibrating Filtration (RVF) module, Separation and Purification Technology, (2021) 118955.

[12] M. Cheng, C. Le Men, A. Line, P. Schmitz, L. Fillaudeau, Investigation of instantaneous and local transmembrane pressure in rotating and vibrating filtration (RVF) module: Comparison of three impellers, Separation and Purification Technology, 280 (2022) 119827.

[13] J. Murkes, C.G. Carlsson, Crossflow filtration: Theory and practice, (1988).

[14] X. Xie, C. Le Men, N. Dietrich, P. Schmitz, L. Fillaudeau, Local hydrodynamic investigation by PIV and CFD within a Dynamic filtration unit under laminar flow, Separation and Purification Technology, 198 (2018) 38-51.

[15] L.O. Wilson, N.L. Schryer, Flow between a stationary and a rotating disk with suction, Journal of Fluid Mechanics, 85 (2006) 479-496.